AIAA JOURNAL
Vol. 46, No. 1, January 2008

Design Optimization of a Controllable Camber Rotor Airfoil

Farhan Gandhi,* Mary Frecker,† and Andrew Nissly‡
Pennsylvania State University, University Park, Pennsylvania 16802

DOI: 10.2514/1.24476

A conformable airfoil is proposed as an alternative to trailing-edge flaps used for active helicopter vibration reduction through high-frequency changes in camber. The design consists of several compliant mechanisms of predetermined topology that are placed serially within the airfoil along the chord, aft of the leading-edge spar. A shape optimization approach is used to design the compliant mechanisms, in which the objective is to maximize trailing-edge deflection while minimizing airfoil deflections due to aerodynamic loads. Solutions were obtained using a sequential linear programming method coupled with a finite element analysis. An optimized shape is predicted to achieve a trailing-edge deflection of ±6.0 mm or a ±4.6-deg equivalent flap deflection angle using the tip deflection objective. Results indicate that the deflection is dependent on the amount of passive material allowed and the objective function used. The aerodynamic loads are found to cause only small deformations in comparison with those caused by the actuation. Prototype fabrication and bench-top tests demonstrated that rotor airfoil camber is controllable using the proposed concept.

Introduction

THE blades of the main rotor of a helicopter are slender and flexible along the span, but stiff along the cross section. The airfoil cross section is essentially rigid because any change in the airfoil shape due to aerodynamic loading could significantly affect the aerodynamic performance. Although an uncommanded change in airfoil profile would obviously be undesirable, an intentionally introduced change in airfoil shape could be used, even exploited, in a number of ways. Although a steady (nonoscillatory) or a once-per-revolution change in cross-sectional shape could be used to improve performance over a range of operating conditions, a higher harmonic variation in the airfoil profile could be used to decrease vibratory loads. In this respect, a continuously deformable or conformable rotor blade airfoil would be a successor to rotor blade airfoils with trailing-edge (TE) flaps, which have been extensively considered for helicopter vibration reduction over the last decade [1–11]. Virtually all of the research efforts focusing on rotor TE flaps for vibration reduction have used actuators constructed from piezoelectric material to deflect the flaps because these actuators are solid state, compact, and can produce the required force at high frequency. However, the stroke of piezoelectric actuators is usually very small, and so a mechanical amplification of the stroke is necessary. Examples of these actuator–amplifier mechanisms include double-L piezostack actuators [5], C-block actuators [6,7], X-frame actuators [8], and bimorph-lever benders [10,11]. Continuously conformable rotor airfoils will also be required to use a piezoelectric-based actuation system to meet the frequency requirements. Other solid-state-actuation concepts based on "smart" materials such as shape memory alloys (SMAs) do not have the required frequency bandwidth to provide cyclic actuation over every rotor revolution even though they can provide a larger stroke. As with trailing-edge flaps, design optimization of the actuator and amplification mechanism could produce the required stroke amplification. The idea of using such a smart-materials-based continuously conformable rotor airfoil was first suggested by Ormiston in the early 1990s.

Received 11 April 2006; revision received 8 June 2007; accepted for publication 2 July 2007.

*Professor, Department of Aerospace Engineering, 231C Hammond Building. Senior Member AIAA.
†Professor, Department of Mechanical and Nuclear Engineering, 326 Leonhard Building.
‡Research Assistant, Department of Mechanical and Nuclear Engineering, 332 Leonhard Building.

Continuously deformable airfoils have already been considered for performance and handling-quality improvement of fixed-wing aircraft (quasi-static or low-frequency actuation required). For example, Saggere and Kota [12] suggested the use of passive compliant structures with a generic force actuator to produce static shape control of an airfoil camber. Other shape optimization approaches for compliant-mechanism design have been proposed by Hetrick and Kota [13] and Xu and Ananthasuresh [14]. Rediniotis et al. [15] considered the design of a reconfigurable wing actuated by SMA wires to maximize the lift-to-drag ratio. Kudva et al. [16], as a part of the Defense Advanced Research Projects Agency (DARPA)-sponsored Smart Wing program, developed deformable airfoil surfaces using ultrasonic piezoelectric motors and demonstrated that the airfoil could achieve trailing-edge deflections of up to 20 deg. Raney et al. [17] designed and tested a smooth adaptive wing using SMA actuators. Achievable deflections were reported to be 8 and 3 deg for the trailing edge and leading edge, respectively. Despite the significant deflections, the SMA-based actuators may not be suitable for rotor vibration reduction due to their bandwidth limitation. Anusonti-Inthra et al. [18] conducted research on conformable rotor airfoils using an optimized ground structure of piezoelectric elements. Predicted trailing-edge deflections were 4 deg, but the structure required a very large number of piezoelectric elements. In the current study, we propose a conformable rotor airfoil design consisting of a passive compliant structure coupled with a limited number of piezoelectric actuators to reduce the complexity of the design.

The objective of the present study is to develop an appropriate optimization methodology and to use it for the design of a smart-materials-based conformable airfoil for a helicopter main rotor blade. In this study, several compliant mechanisms of predetermined topology are placed serially within the airfoil along the chord, aft of the leading-edge spar. As with the active flap concepts, active vibration control can be achieved by changing the aerodynamic loads on the airfoil through high-frequency changes in camber. In the conformable airfoil, the compliant-mechanism structure and actuators are entirely contained within the airfoil cross section, thereby reducing aerodynamic drag and power penalties. Additionally, the compliant mechanisms allow deformation without the complexity associated with mechanical hinges, linkages, and numerous moving parts. The optimally designed conformable rotor airfoil is fabricated, and bench-top tests are conducted to demonstrate the camber variation predicted by simulation.

Analytical Model

A NACA-0012 airfoil was selected as the baseline airfoil for camber variation because it is simple, symmetric, and its

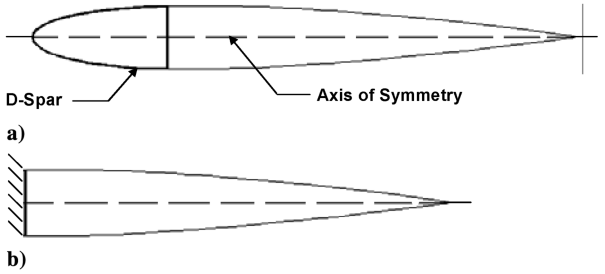

Fig. 1 Schematic representation of a) NACA-0012 airfoil rotor blade section with leading-edge D-spar, and b) Design domain for optimization, aft of the rigid D-spar.

aerodynamic properties are well-documented [19]. A rotor blade cross section with a NACA-0012 airfoil is shown in Fig. 1a. The blade airfoil section is assumed to have a chord length of 0.5 m (1.66 ft). A rigid D-spar serves as the primary load-carrying member and is located in the region extending from the leading edge to the quarter-chord. The rigid D-spar is assumed to undergo no chordwise deformation under any loading conditions considered in this work. This condition is enforced in the analysis by assuming the compliant section aft of the spar to be clamped at the quarter-chord (Fig. 1b). As a result, the design domain for the optimization problem is defined as the region enclosed by the airfoil geometry between the quarter-chord and the trailing edge.

The design domain is parameterized using a series of simple compliant mechanisms of predetermined topology. A small number of actuators within the airfoil cross section are used in conjunction with the compliant mechanisms to expand and shrink the top and bottom skins of the airfoil, thereby producing camber variation. The topology of the mechanism used is shown in Fig. 2a. This topology was selected because several mechanisms could be placed in series along the chord within the airfoil, and the mechanism amplifies the stroke of the actuator. The vertical members in Fig. 2a are the active elements (piezoelectric stack actuators), and the inclined members are passive structural elements. When the top actuators contract and the bottom actuators synchronously expand, the mechanism deforms into a configuration shown in Fig. 2b. In the figure, the passive links rotate relative to one another and to the actuator elements, but the actuator elements do not rotate relative to one another.

An analogous compliant mechanism can be realized by simply replacing the rigid links and pin joints with a passive compliant structure. By placing several units in series along the chord of the airfoil cross section, as shown in Fig. 3a, the deformation of each unit is additive and results in a large change in camber.

The topology of the compliant mechanism is unchanged and a shape optimization of the compliant structures is performed. Continuous shape optimization is approximated by sizing the in-plane thickness t_i of the discrete elements, as shown in Fig. 3b. The design variables in the optimization problem are the thicknesses t_i of the elements that make up the top half of the passive substructures (each compliant member consists of 12 elements, as shown in Fig. 3b). The structure is constrained to be symmetric about line A–B (Fig. 2a) so that the trailing-edge deflections will be equal and opposite when opposite voltages are applied to the actuators. The passive elements are assumed to have a Young's modulus of 60 GPa, and the active elements are modeled as induced strain piezoelectric actuators also having a Young's modulus of 60 GPa and a maximum free strain of 1%. With actuation frequencies in the range of 20 Hz required for vibration reduction in full-scale rotors (and even higher frequencies required for model rotors), piezoelectric actuators are a good selection because of their fast response time. The stack actuator configuration, using the d_{33} effect, is chosen for its high force output. Each piezoelectric stack actuator is modeled as a single active truss element (two displacement degrees of freedom per node). The skin of the airfoil and the passive compliant-mechanism structure are discretized using plane frame elements that allow for bending and extensional deformations (two displacement degrees and one rotation degree of freedom per node).

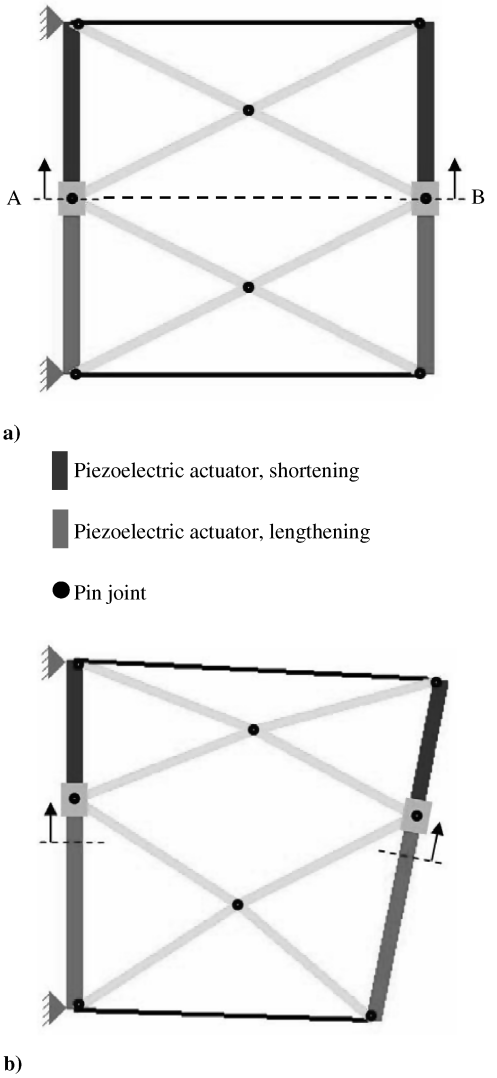

Fig. 2 Rigid link mechanism in a) unactuated and b) actuated configuration.

The analysis of two different loading conditions is necessary for the formulation of the shape optimization problem: 1) the forces generated by the piezoelectric actuators and 2) the aerodynamic forces acting on the airfoil. A description of the application of these forces in the formulation of the optimization problem is provided in this section.

An equivalent force due to the expansion of the piezoelectric elements distributed within the airfoil is calculated and defined as f_{act}. The application of a voltage V to a piezoelectric element generates an equivalent axial load, which is defined in Eq. (1):

$$f_{\text{act}} = \frac{EAd_{33}V}{L} \tag{1}$$

where E is the modulus of elasticity of the piezoelectric material (N/m^2), A is the piezostack actuator cross-sectional area (m^2), d_{33} is the piezoelectric strain constant (m/V), and L is the length of the actuator (m).

Positive airfoil camber corresponds to downward deflection of the trailing edge, and the magnitude of the camber corresponds to the vertical displacement u_{tip} of the airfoil trailing edge, as shown in Fig. 3a.

The passive compliant structure, along with the piezoelectric and skin elements, must be sufficiently stiff to avoid undesired airfoil deformations due to the aerodynamic pressure loads on the upper and lower surfaces of the airfoil. The pressure distribution of a two-dimensional airfoil can be numerically calculated using a linear-

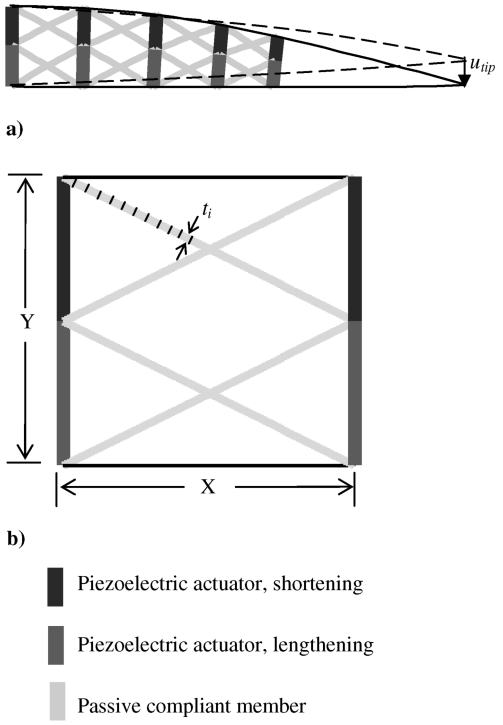

Fig. 3 Illustrations of a) compliant-mechanism units assembled in series along the chord, resulting in camber of the airfoil cross section, b) single undeformed compliant-mechanism unit.

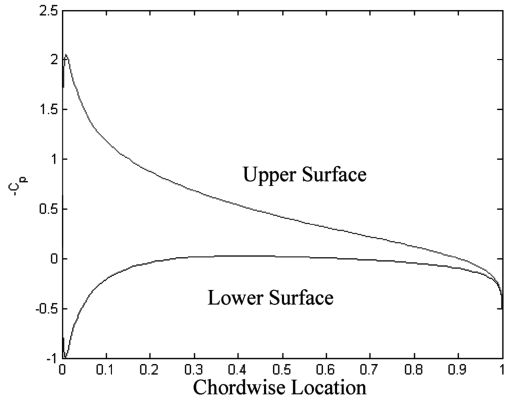

Fig. 4 Pressure coefficient for a NACA-0012 airfoil at 5-deg angle of attack.

strength vortex method. This two-dimensional panel method includes the effects of the airfoil thickness, angle of attack, and mean-camber line in the calculation of the aerodynamic pressure distribution. A detailed explanation of this method is given by Katz and Plotkin [20]. A sample nondimensional pressure distribution calculated using a NACA-0012 airfoil at an angle of attack of 5 deg is shown in Fig. 4. The figure shows the pressure coefficients C_p corresponding to the top and bottom surfaces.

The aerodynamic force acting on the skin elements is calculated from the coefficient of pressure distribution. The dimensional pressure on the ith skin element can be calculated using

$$p_i = \tfrac{1}{2}\rho V_\infty^2 C_{pi} \tag{2}$$

where C_{pi} is the pressure coefficient, V_∞ is the freestream velocity, and ρ is the air density. A velocity of 200 m/s (Mach 0.6) is selected as the reference freestream velocity for the aerodynamic load calculations. The aerodynamic load f_i on each skin element is then given by

$$f_i = p_i w_i l_i \tag{3}$$

where l_i is the length of the element along the airfoil cross section and w_i is the width along the span. From the distributed aerodynamic load on each skin element, the finite element nodal loads are calculated as

$$f_{\text{air}}^i = L^T\left[0, \frac{f_i l_i}{2}, \frac{f_i l_i^2}{12}, 0, \frac{f_i l_i}{2}, -\frac{f_i l_i^2}{12}\right] \tag{4}$$

where the transformation matrix L, required to account for the orientation of the skin elements, is defined as

$$L = \begin{bmatrix} c & s & 0 & 0 & 0 & 0 \\ -s & c & 0 & 0 & 0 & 0 \\ 0 & 0 & 1 & 0 & 0 & 0 \\ 0 & 0 & 0 & c & s & 0 \\ 0 & 0 & 0 & -s & c & 0 \\ 0 & 0 & 0 & 0 & 0 & 1 \end{bmatrix} \tag{5}$$

and c and s are the direction cosines determined from the nodal coordinates x_1, x_2, y_1, and y_2:

$$c = \cos\theta = \frac{x_2 - x_1}{l} \qquad s = \sin\theta = \frac{y_2 - y_1}{l} \tag{6}$$

Although the aerodynamic loads would vary as the airfoil deforms under actuation, these variations are not considered in calculating f_{air} in Eq. (4). This can be justified in the following terms: The reason for calculating the displacement due to airloads is to ensure that as the material distribution within the airfoil section aft of the spar is varied during the design optimization process, the airfoil does not become overly flexible under aerodynamic loading. In this regard, the baseline aerodynamic surface pressure distribution is adequate and considering perturbation in pressure distribution due to variation in camber (which is tantamount to accounting for aerodynamic stiffness) is not expected to a result in a different conclusion.

Optimization Problem

Objective Function

A compliant mechanism must be sufficiently flexible to achieve the desired displacement under actuation. However, it also needs to have sufficient stiffness to transfer force efficiently and resist the external aerodynamic loads acting on the structure. This work seeks to find the optimal passive-material distribution so that the trailing-edge deflection is maximized under the actuation forces and at the same time minimized under the external aerodynamic loads.

The flexibility requirement under actuation is measured in terms of the vertical tip deflection (TD) of the airfoil, in which u_{tip} is the component of u_{act} corresponding to the vertical deflection at the trailing edge. This is obtained by solving the equilibrium equation:

$$Ku_{\text{act}} = f_{\text{act}} \tag{7}$$

where K is the finite element global stiffness matrix of the system. The structural stiffness requirement is measured in terms of the inverse of the strain energy (SE) due to prescribed aerodynamic loads. The strain energy of the compliant airfoil due to deformation u_{air} under aerodynamic loads f_{air} is calculated using

$$\text{SE} = \tfrac{1}{2}u_{\text{air}}^T K u_{\text{air}} \tag{8}$$

where u_{air} is obtained from

$$Ku_{\text{air}} = f_{\text{air}} \tag{9}$$

The combination of the flexibility and stiffness requirements results in a multiple criteria design problem, in which the two apparently conflicting criteria need to be satisfied simultaneously. The formulation of this type of problem can be accomplished using a ratio-type objective function proposed by Frecker et al. [21]. Using this approach, the objective function is defined as the ratio of the tip

deflection under actuation to the strain energy due to deformation under aerodynamic loads, as shown in Eq. (10):

$$\max\left(\frac{\text{TD}}{\text{SE}}\right) = \left(\frac{-(u_{\text{act}})_{\text{tip}}}{u_{\text{air}}^T K u_{\text{air}}}\right) \tag{10}$$

subject to

$$Ku_{\text{act}} = f_{\text{act}} \qquad Ku_{\text{air}} = f_{\text{air}} \qquad \sum_{i=1}^{n} t_i l_i \leq A_{\text{upper}}$$

$$t_{\min} \leq t_i \leq t_{\max}$$

The design problem was also solved using a single-criteria objective of only the tip deflection due to actuation as shown in Eq. (11):

$$\max(\text{TD}) = u_{\text{tip}} \tag{11}$$

For both objective functions, the upper limit on the amount of passive material, A_{upper}, is defined as some percentage of the maximum possible total area:

$$A_{\max} = \sum_{i=1}^{N} l_i t_{\max}$$

A_{upper}, used to limit the amount of passive material allowed, is similar to volume constraints typically used in topology and shape optimization problems. The thicknesses t_i of the passive elements are used as the design variables in the shape optimization problem. The lower limit on the design variable $t_{\min}$ is set to a small number based on the minimum thickness to ensure the manufacturability of the final design. The upper bound on the design variables, $t_{\max}$, is selected by inspecting the physical space available in the design domain. The effect of altering this parameter is discussed in the Results and Discussion section. Neither the skin elements, nor the piezoelectric elements, both of which provide passive structural support, are optimized in the design problem. That is, the skin and piezoelectric element cross-sectional areas remain constant through the shape optimization procedure.

Finite Element Analysis Formulation

The design formulation of the previous sections is implemented using linear finite element analysis coupled with the sequential linear programming (SLP) method to solve the optimization problem. Linear finite element analysis is appropriate in this case because the deformations are small. The global stiffness matrix for the structure is assembled by the usual finite element analysis procedure using the elemental stiffness matrices of the frame and truss elements.

Sequential Linear Programming

In this work, the shape optimization problem is solved using the SLP method, in which the nonlinear objective function is linearized using a Taylor's series expansion, and a small move limit is imposed on the design variables. This method is selected because it is computationally inexpensive. The SLP method is guaranteed to converge for convex problems and has the ability to incorporate both equality and inequality constraints. For problems that are not convex, the SLP algorithm is likely to find a local maximum. For this reason, several different randomly generated starting points were used, as described later in this paper. The SLP method requires the calculation of the sensitivities of the objective function. The sensitivities are calculated analytically and can be found in the Appendix.

A MATLAB code was written to implement the SLP algorithm, including the finite element analysis and sensitivity calculations. The computational procedure is shown schematically in Fig. 5. The user is required to enter the material and geometric properties of the structure, including the aspect ratio of the compliant-mechanism unit (defined as the ratio of the width to the height of the unit, X/Y in Fig. 3b), the width of the piezoelectric actuator elements, and the stiffness of the skin.

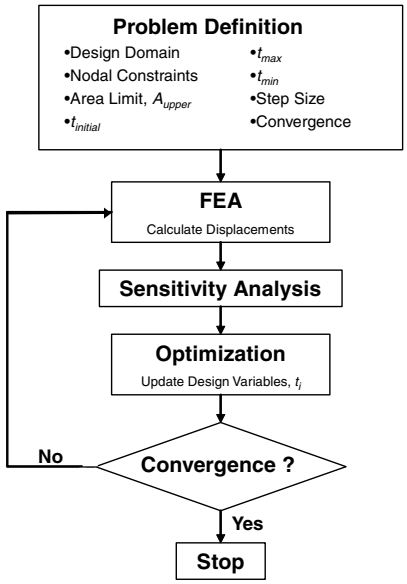

Fig. 5 SLP algorithm.

The algorithm was configured to generate a random feasible starting point. The iterative process to obtain a solution is as follows: First, the algorithm calculates the nodal deflections of the structure using linear finite element analysis and the loading conditions defined previously. Then the sensitivities of the objective function are calculated using the expressions in the Appendix. The linear subproblem is solved using the `linprog` function in the MATLAB optimization toolbox, which uses an interior point method. The design variables and objective function are updated, resulting in a new distribution of passive material. These steps are repeated until convergence is achieved, which is defined as four successive iterations in which the objective function changes by less than 0.1%.

Additional Calculations

Several calculations are performed on the optimized airfoil that serve as a measure of the design effectiveness and provide a basis for comparison of the conformable airfoil with a conventional trailing-edge flap. The parameters include an effective trailing-edge flap angle and a change in lift created by the change in camber due to actuation.

Effective Trailing-Edge Flap Angle

The main objective of the conformable airfoil is to achieve camber deformations that create significant change in the aerodynamic loads on the airfoil. To quantify the degree of camber achieved by the conformable airfoil, an equivalent flap deflection angle δ_f can be defined based on the trailing-edge vertical deflection of the conformable airfoil u_{tip}. This angle is calculated by assuming that the deflection is obtained from an equivalent trailing-edge flap of chord length equal to 15% of the blade chord c; thus,

$$\delta_f = \tan^{-1}\left(\frac{-(u_{\text{act}})_{\text{tip}}}{0.15c}\right) \tag{12}$$

Airfoil Lift and Drag Coefficients

The change in the lift coefficient created by the airfoil deflection provides a measure of the conformable airfoil effectiveness in modifying the aerodynamic loads. For the conformable airfoil, the change in these coefficients is calculated using the X-FOIL code [22]. For comparison, X-FOIL is also used to calculate the change in lift and drag coefficient for a 15% chord trailing-edge flap. When comparing the incremental lift due to change in camber with that due to trailing-edge flap deflection, the cost incurred, in terms of aerodynamic drag, must also be considered. The X-FOIL code is also

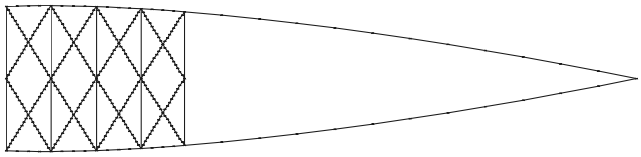

Fig. 6 Initial ground structure parameterization: 450 elements.

used to calculate drag coefficient associated with camber and trailing-edge flap deflections. X-FOIL is a program designed for the analysis of low Reynolds number airfoils. X-FOIL computes lift and drag coefficients using the Karmen–Tsien compressibility correction [22].

Results and Discussion

Ratio Objective Function

Initially, optimization was conducted using the ratio objective function for a ground structure (as shown in Fig. 6, composed of four serially arranged compliant mechanisms, each with an aspect ratio X/Y of 30%) and for $A_{\text{upper}} = 50\%A_{\max}$. The discretized structure contains 450 elements, including 384 inclined passive elements (but only 192 design variables, due to symmetry), 56 skin elements (each skin section between successive actuators is discretized into four elements, and the upper and lower portions of the skin aft of the compliant-mechanism units are discretized into 24 elements), and 10 actuator elements. The skin elements aft of the compliant-mechanism units are included to provide nodes for the calculation of the aerodynamic forces acting on this portion of the airfoil. For the analysis of these elements, we assigned a very high axial stiffness, making this portion of the airfoil essentially rigid. The properties of the airfoil structure are given in Table 1, and the constraints on the design variables are given in Table 2.

A solution is determined by solving the optimization problem using the ratio objective for the ground structure described earlier. The applied voltage V is equal to the maximum driving voltage of ± 1000 V (resulting in approximately 0.15% free strain). The voltage applied to the actuators in the top and bottom halves of the structure is of opposite polarity to result in a downward trailing-edge deflection. The optimization program is executed using a batch of five randomly generated feasible starting points.

For the example considered, the SLP algorithm converges to an optimal solution in approximately 60 iterations, as shown by the convergence history in Fig. 7. The optimized shape obtained is shown in Fig. 8. A downward tip deflection of 3.7 mm is predicted with this optimized shape. This tip deflection is equivalent to a 15% trailing-edge flap deflection angle of 2.84 deg. The tip deflection due to the aerodynamic loads is 0.32 mm.

Several observations can be made from the optimized topology of the initial configuration. First, the solution uses all of the passive material available, by reaching the passive-material area constraint A_{upper}. Figure 9 shows that the tip deflections due to actuation and the aerodynamic loads vary as the optimization process progresses. The reduction in both the actuation and airload deflections indicates that the optimizer is causing the structure to become stiffer as the value of the ratio objective function is increasing.

All of the five randomly generated starting points resulted in nearly identical solutions. This suggests that the topology optimization likely converges to the global optimum and that the solution is independent of the initial guess provided. Thus, for each of the optimization runs presented in the remainder of this paper, only one randomly generated starting point was used.

Next, studies were performed to determine the effect of passive-material area limit A_{upper} and the aspect ratio of the compliant mechanisms (X/Y in Fig. 3b) on the optimized shape of the

Table 1 Properties of airfoil structure

Parameter	Value
Actuator Young's modulus	60×10^9 N/m^2
Actuator free strain	0.15%
Actuator thickness	3 mm
Airfoil chord	0.5 m
Airfoil skin bending stiffness	60 N-m
Airfoil skin axial stiffness	6×10^5 N/m
Passive-structure Young's modulus	60×10^9 N/m^2

Table 2 Passive-material constraints

Thickness of passive members	Value
Maximum, $t_{\max}$	7 mm
Minimum, $t_{\min}$	0.001 mm

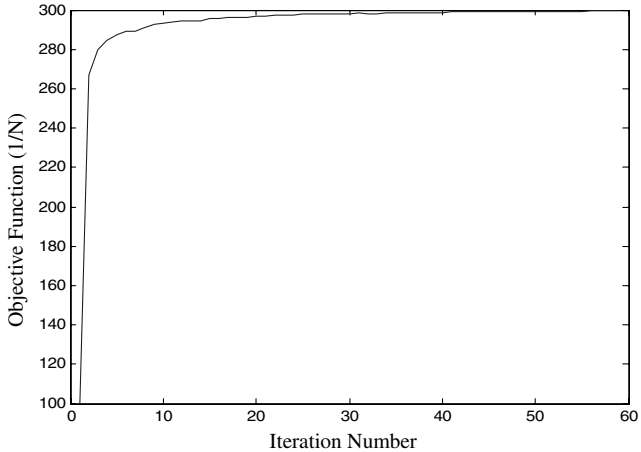

Fig. 7 Convergence history.

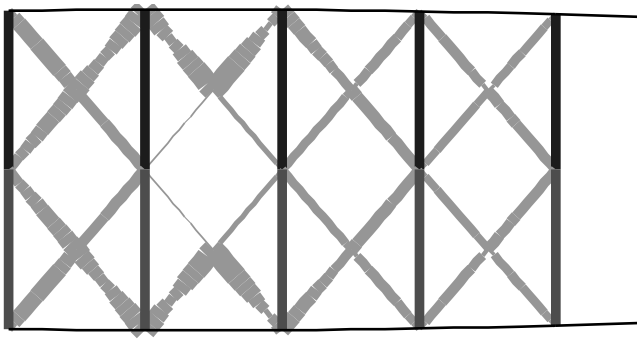

Fig. 8 Optimized shape using ratio objective function with $X/Y = 30\%$ and $A_{\text{upper}} = 50\%A_{\max}$.

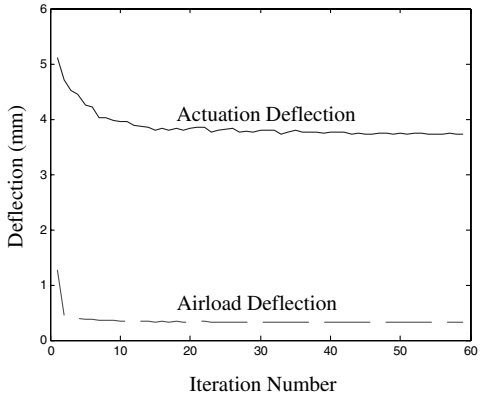

Fig. 9 Actuation and airload deflections as optimization using ratio objective function progresses.

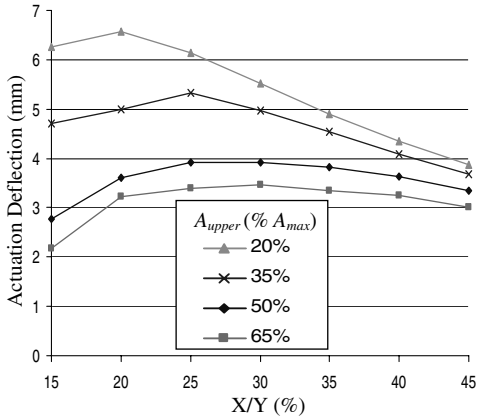

Fig. 10 Tip deflection due to actuation, versus compliant-mechanism aspect ratio, for several A_{upper} values (results from optimization using the ratio objective function).

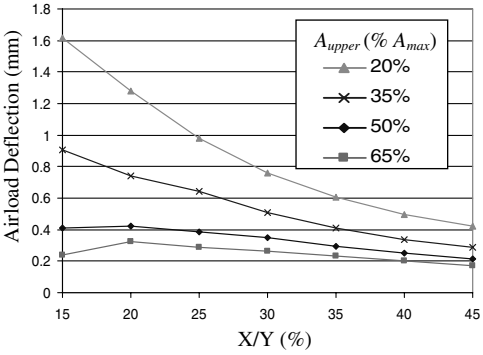

Fig. 11 Tip deflection due to airloads versus compliant-mechanism aspect ratio, for several A_{upper} values (results from optimization using the ratio objective function).

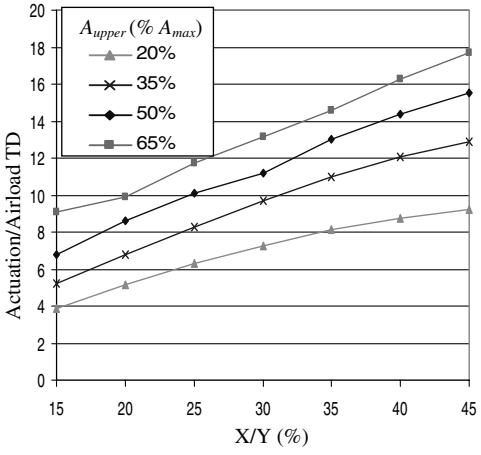

Fig. 12 Ratio of tip deflection due to actuation/tip deflection due to airloads versus compliant-mechanism aspect ratio, for several A_{upper} values (results from optimization using the ratio objective function).

compliant mechanisms and their performance. Figures 10 and 11 show the actuation and airload deflections, respectively, as a function of compliant-mechanism aspect ratio, for different passive-material area limits, and Fig. 12 shows the ratio of the tip deflection due to actuation to the tip deflection due to airloads. It is observed that for maximum actuation deflection, the best mechanism aspect ratio is between 20–30%, and low values of A_{upper} are preferred. However, a lower aspect ratio and A_{upper} also result in a more flexible airfoil (Fig. 11) and the ratio of actuation to airload tip deflection is poorest.

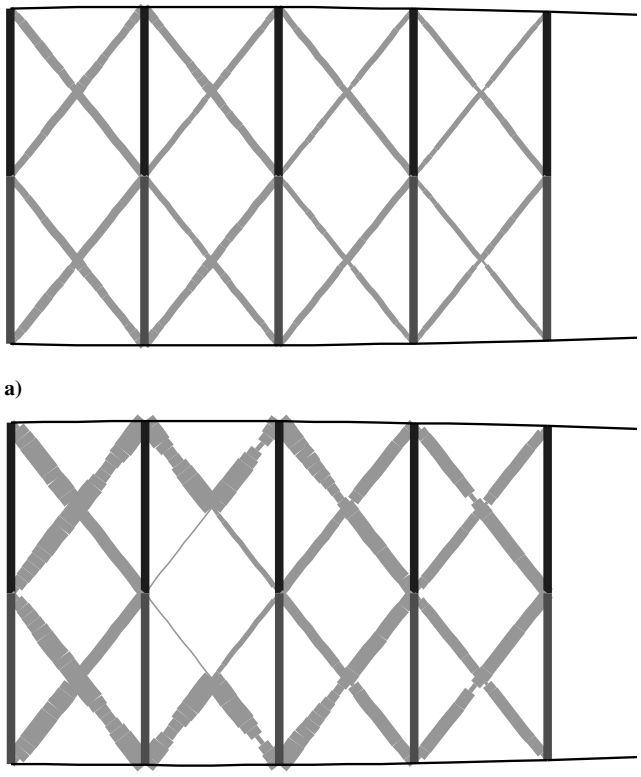

Fig. 13 Optimized compliant-mechanism shape using ratio objective function for A_{upper} of a) 35% and b) 65%A_{max} values.

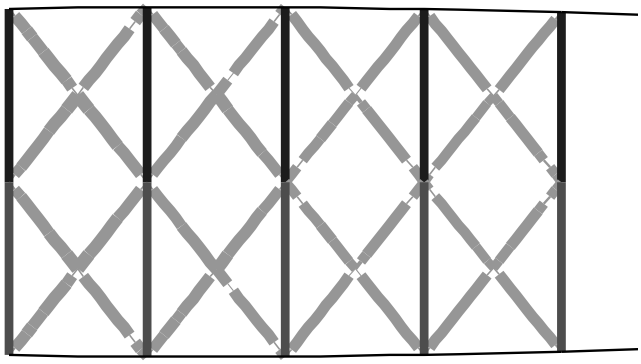

Fig. 14 Optimized shape using TD objective function with $X/Y = 30\%$ and $A_{\text{upper}} = 50\%A_{\text{max}}$.

This ratio is best for highest values of A_{upper} and stiffer airfoils (Fig. 12), even though the actuation deflections are reduced.

The optimized shape using the ratio objective function varied depending on the passive-material area constraint used. Figure 13 shows that as A_{upper} is increased, the passive material changes from a nearly uniform to a highly nonuniform distribution, with material concentrated toward the leading-edge spar (and for the second unit, concentrated closer to the skin) while using much less material near the midplane.

TD Objective Function

This section provides optimization results using the TD objective function. As with the ratio objective function, the 30% aspect ratio compliant mechanism and $A_{\text{upper}} = 50\%A_{\text{max}}$ case is considered first. Again, convergence occurs in approximately 60 iterations and the passive material reaches the upper limit A_{upper}. Figure 14 shows the corresponding optimized shape, which appears very different from

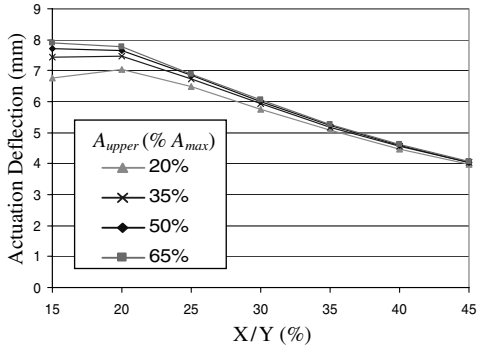

Fig. 15 Tip deflection due to actuation, versus compliant-mechanism aspect ratio, for several A_{upper} values (results from optimization using the TD objective function).

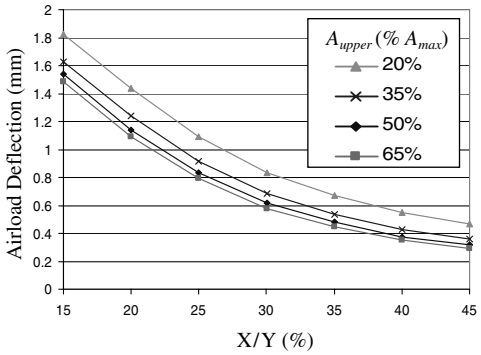

Fig. 16 Tip deflection due to airloads, versus compliant-mechanism aspect ratio, for several A_{upper} values (results from optimization using the TD objective function).

that obtained using the ratio objective (Fig. 8). In the present case, the compliant mechanisms have a mostly uniform distribution of material except at the ends of many of the "individual links," in which thin flexurelike elements are seen to develop. These flexures act as virtual hinges. The deflections due to actuation and airloads for this solution are 6 and 0.6 mm, respectively.

Next, the passive-material limit A_{upper} and the compliant-mechanism aspect ratio are varied. Figure 15 shows that as the aspect ratio (X/Y) increases, the tip deflection under actuation decreases. This is attributed to the compliant mechanism, with lower aspect ratios having a greater geometric advantage. Also, as A_{upper} increases, there is a small increase in tip deflection because the stiffer individual passive links are better able to transmit the force required to stretch the airfoil skin. It should be noted that again the optimized structures reached the allowable passive-material area limit A_{upper}. Figure 16 shows that as the compliant-mechanism aspect ratio increases, the deflection due to the aerodynamic loads decreases. The ratio of deflection due to actuation to the deflection due to the aerodynamic loads (Fig. 17) increases as the compliant-mechanism aspect ratio and the passive-material area A_{upper} increase. Optimized geometries for different A_{upper} values are shown in Fig. 18 and it is observed that the geometries are similar to that in Fig. 14, the only difference being the relative thickness of the passive elements, with change in the value of A_{upper}.

Comparison of Ratio and TD Objective Functions

Comparing Figs. 13a and 18a, it is observed that for a low passive-material area constraint, $A_{\text{upper}} = 35\%A_{\text{max}}$, the optimized designs using the TD and ratio objective functions are very similar. On the other hand, for a high passive-material area constraint, $A_{\text{upper}} = 65\%A_{\text{max}}$, the optimized designs using the two objective functions differ substantially (compare Figs. 13b and 18b). Figures 19 and 20 compare the deflections due to actuation and aerodynamic loads, respectively, for the two objective functions for

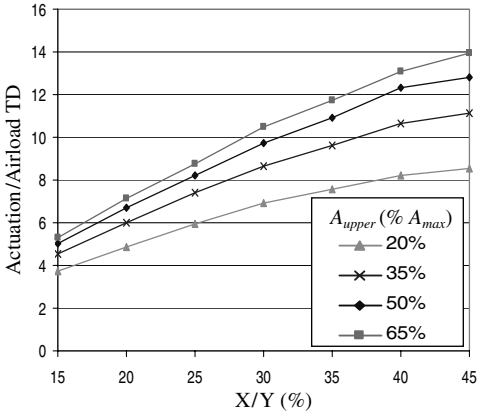

Fig. 17 Ratio of tip deflection due to actuation / tip deflection due to airloads versus compliant-mechanism aspect ratio, for several A_{upper} values (results from optimization using TD objective function).

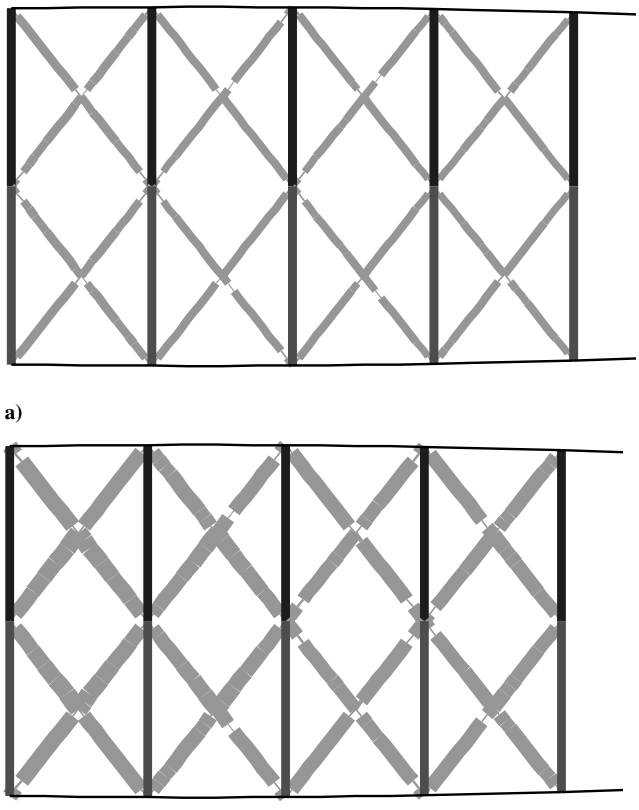

Fig. 18 Optimized compliant-mechanism shape using TD objective function for A_{upper} of a) 35% and b) 65%A_{max} values.

low and high values of A_{upper}. For a low value of $A_{\text{upper}} = 20\%A_{\text{max}}$, the actuation deflection (Fig. 19) and the airload deflection (Fig. 20) from the two optimization methods are similar, because the compliant-mechanism designs themselves were similar. For a high value of $A_{\text{upper}} = 65\%A_{\text{max}}$, the actuation deflection (Fig. 19) and the airload deflection (Fig. 20) using the TD objective function do not show much change, but those using the ratio objective show a significant reduction. This is because with the TD objective, recall that the optimized design did not change much (examine Fig. 18), but with the ratio objective, the optimized design became much stiffer (Fig. 13).

The ratio of the deflection due to actuation to the deflection due to the aerodynamic loads (Figs. 12 and 17) is higher in all cases when using the ratio objective function, but the individual deflections

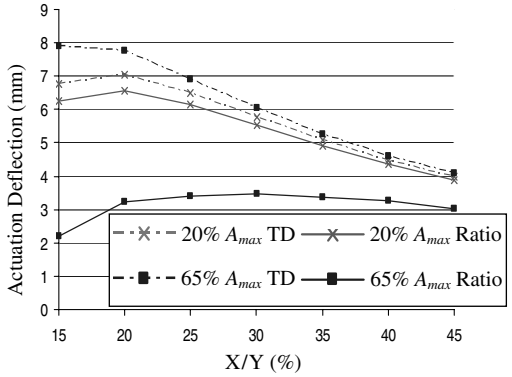

Fig. 19 Comparison of actuation deflections for TD and ratio objective functions.

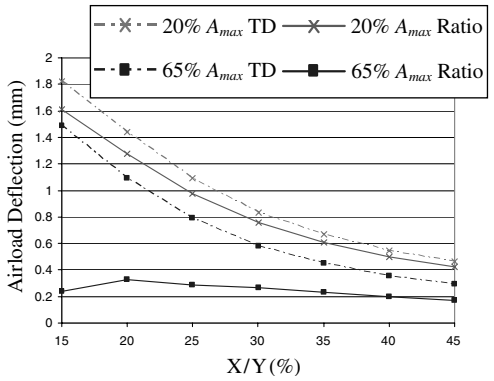

Fig. 20 Comparison of airload deflections for TD and ratio objectives functions.

themselves are lower. If larger actuation deflections are desired, it may be reasonable to select a design obtained using the TD objective. The structure would be more flexible and even though the deflections under the aerodynamic loads would be higher, this may be acceptable, provided they remain below a certain threshold. Ease of construction is another consideration that may lead to the selection of TD objective function designs.

Effect of Actuator Thickness

In the preceding sections, a constant piezoelectric actuator thickness of 3 mm was used in the simulations. This section examines the effect of varying the actuator thickness. A set of four compliant-mechanism units having an aspect ratio of $X/Y = 30\%$ and a passive-material limit of $A_{\text{upper}} = 50\% A_{\max}$ was used. As shown in Fig. 21, the actuator thickness had very little effect on the actuation and airload deflections in the design obtained using the TD objective function. This suggests that the actuator is operating close to its free-strain value even when it is at the smallest thickness. For the ratio objective, however, the optimized shape is much stiffer, to decrease the deflection due to the aerodynamic load. In this case, the tip deflection due to actuation increases noticeably with an increase in actuator thickness, because the thicker actuators provide additional force. For both objectives, as the actuator thickness increases, the deflection due to the aerodynamic loads decreases. The effect of actuator thickness on the aerodynamic deflection is more pronounced for the TD objective function, because the optimized designs using this objective function tend to be more compliant. The optimized shape of the passive material does not change with the actuator thickness.

Change in Lift and Drag Coefficient

The main objective of the conformable airfoil designed in this work is to generate changes in the aerodynamic loads of the blades to reduce rotor vibrations. The change in aerodynamic loads can be

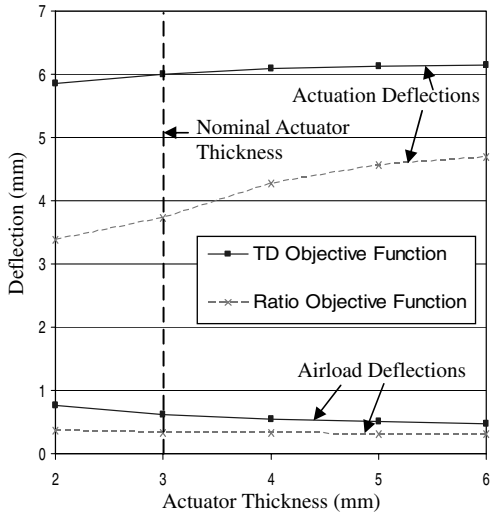

Fig. 21 Effect of actuator thickness on deflections for TD and ratio objective functions.

measured as the change in lift coefficient due to a modified pressure distribution. For both the conformable airfoil and the trailing-edge flap airfoil, the coefficients of lift and drag are calculated numerically using the program X-FOIL.

Figure 22 shows the percentage lift coefficient change for a NACA-0012 airfoil fitted with a 15% chord trailing-edge flap and for a conformable airfoil achieving equivalent deflections through camber variations. Both airfoils are set at a 5-deg angle of attack so that there is a positive lift coefficient value at the zero flap deflection angle. As shown by the figure, the flapped airfoil generates a larger increase in lift for the same equivalent deflection coming from camber, indicating that more deflection of the conformable airfoil is needed to generate a comparable increment in lift.

The increase in drag coefficient for both airfoils is shown in Fig. 23. The 15% chord trailing-edge flap airfoil produces considerably greater drag than the conformable airfoil (and the X-FOIL analysis did not even take into account any physical gap in the flapped airfoil and associated losses).

Prototype Design, Fabrication, and Bench-Top Test

Based on the shape optimization results, a controllable camber airfoil prototype is designed, fabricated, and actuated to demonstrate camber change in a bench-top test.

Design and Construction of the Prototype Airfoil

The design of the prototype is based on the optimized results using a 30%-aspect-ratio compliant mechanism, a passive-area limit of $A_{\text{upper}} = 50\% A_{\max}$, and the TD objective function. This selection was based on the large deflection due to actuation, the relatively small deflection under the aerodynamic load, and the simplicity of the design (uniform compliant mechanisms, each with constant-thickness "links" and end flexures). The optimized shape of the compliant mechanism for this design is shown in Fig. 14. The dimensions for the prototype, such as the thickness of the compliant links and the flexures, came from the MATLAB optimization results. However, because the optimization code discretizes the compliant section into small elements and the abrupt changes in thickness in the resulting designs introduce stress concentrations, fillets are added to the model to facilitate fabrication and reduce stress. The fillet radius was set at 0.5 mm because it was small enough to make the prototype part as close to the optimal design as possible while still being large enough to machine by wire electrodischarge machining (EDM). Figure 24 shows the Pro-Engineer model of the airfoil profile and compliant mechanisms.

The compliant-mechanism and airfoil portions of the prototype were constructed from a $\frac{1}{2}$-in. T-6061 aluminum plate. A NACA-0012 profile was used to define the airfoil geometry in the prototype.

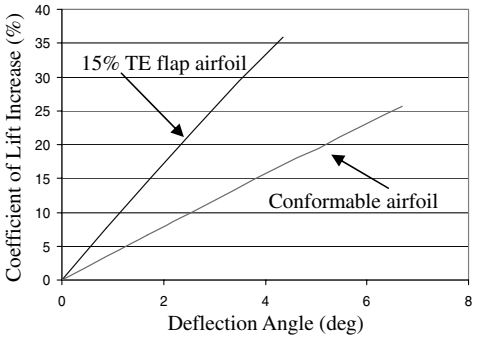

Fig. 22 Percentage increase in lift coefficient as a function of deflection angle for a 15% trailing-edge flap and actively conformable airfoil.

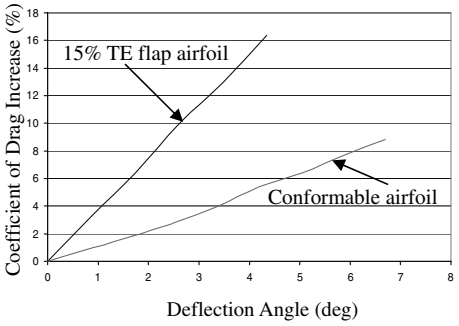

Fig. 23 Percentage increase in drag coefficient of drag as a function of deflection angle for a 15% trailing-edge flap and actively conformable airfoil.

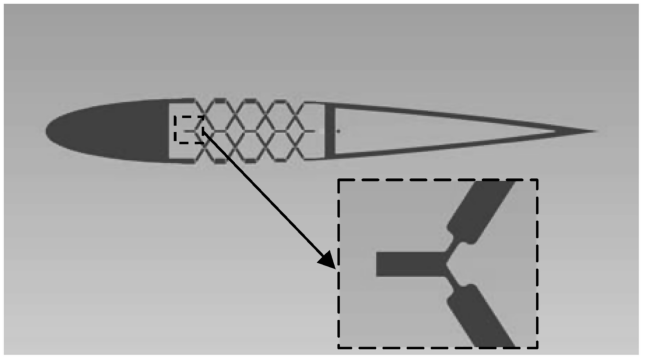

Fig. 24 Pro-Engineer model of the compliant mechanisms within the airfoil.

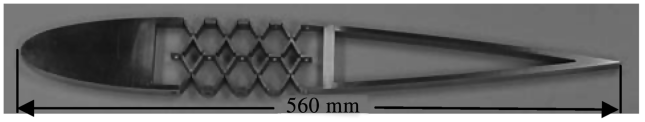

Fig. 25 Fabricated airfoil with compliant mechanisms.

The prototype was machined using wire EDM. Figure 25 shows the completed part.

Actuator Selection

The actuators selected for the prototype were P-010.20H PICA-Thru Piezo Stack Actuators made by Physik Instrumente. The actuators are tubular in shape, allowing for easy assembly in the

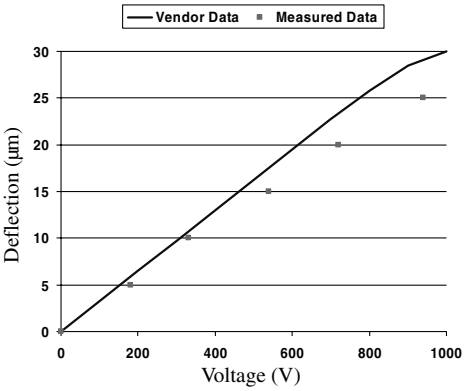

Fig. 26 Actuator tip displacement.

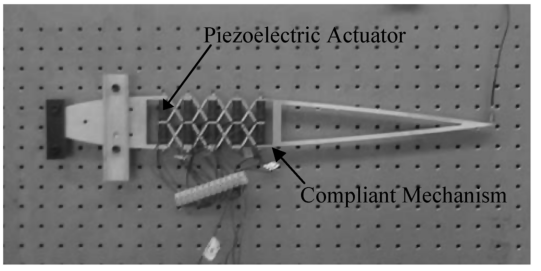

Fig. 27 Assembled prototype with piezostack actuators.

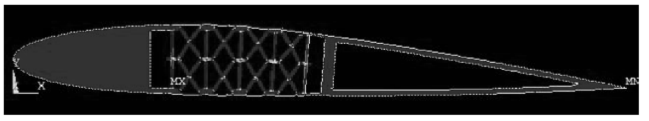

Fig. 28 ANSYS stress analysis.

model. The actuators are 27 mm long with an outer diameter of 10 mm and an inner diameter of 5 mm and are made out of PIC 151 PZT ceramic material. The manufacturer-specified maximum free displacement of the actuators is 30 μm (at a maximum voltage of $+1000$ V), which corresponds to a maximum strain of 0.111%. The actual displacement of the actuators was measured for voltages ranging from 0 to 1000 V. The displacement of the actuators was measured by using an optoNCDT 1800 laser measurement system. The measured actuator displacement versus voltage, as well as the vendor data, is shown in Fig. 26. The average d_{33} value for the 10 actuators found experimentally was $4.05\text{E}-12$ m/V, compared with $4.5\text{E}-12$ m/V as given by the vendor (11.1% difference). The vendor-specified blocked force of each actuator is 1800 N.

The 10 piezostacks are held in place using five 4-mm-diam rods through the holes in their centers. The ends of these rods are threaded and nuts are used on either end to introduce precompression in the actuators. The assembled prototype is shown in Fig. 27.

Stress Analysis

A finite element model of the prototype complete with piezoelectric actuators was set up using ANSYS to ensure that the stresses when the maximum voltage is applied to the piezoelectric actuators are not excessive. The ANSYS model used 72,608 PLANE42-type elements. The model was rigidly constrained at the D-spar. The loading was applied using a thermal load to represent the piezoelectric effect. The ANSYS Von Mises stress analysis results for the entire structure are shown in Fig. 28, and a close-up of the stresses in the flexures is shown in Fig. 29. The ANSYS analysis predicts that the maximum stress in the flexures is 35 MPa, well below the 95 MPa fatigue stress limit of T-6061 aluminum.

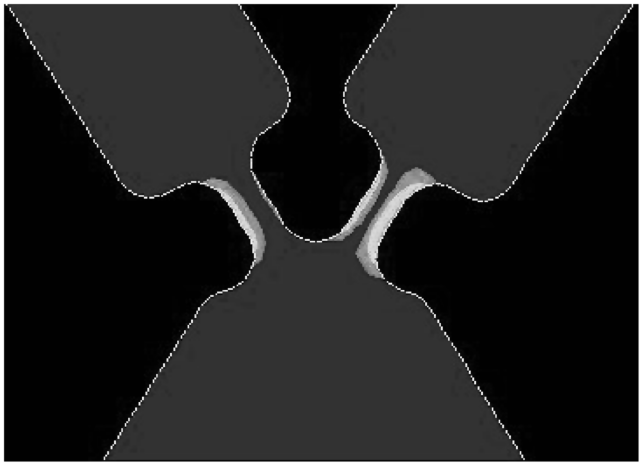

Fig. 29 Close-up of stresses in flexures.

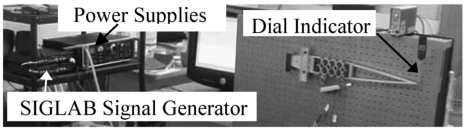

Fig. 30 Test setup.

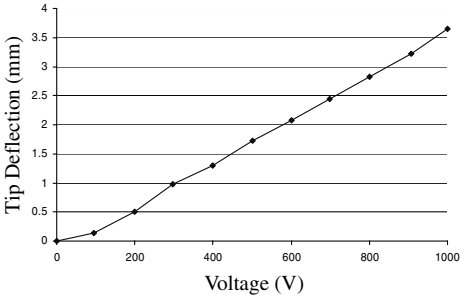

Fig. 31 Measured tip displacement versus top actuator voltage.

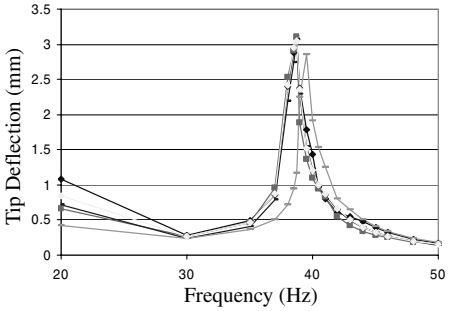

Fig. 32 Measured frequency response function.

The analysis within the MATLAB optimization code was updated to match the prototype by changing parameters such as the free strain of the actuators and the modulus of elasticity of aluminum. The result was a predicted tip deflection under the maximum voltage of 4.1 mm. The maximum tip deflection predicted by the ANSYS model was 3.69 mm. The difference in predicted displacement is attributed to small differences in geometry between the two models. Specifically, the MATLAB analysis represented the piezostack actuators by lines and did not consider their thickness.

Static Test

The test setup for the static testing is shown in Fig. 30. For this test, SIGLAB was used to generate the voltage signals for the top and bottom actuators. These signals were sent to the power supplies in which they were amplified to the required voltage and then sent to the top and bottom actuators. The tip displacement was measured using a dial indicator. For the test, a bias voltage of 500 V was applied to both the top and bottom actuators. This precompressed the stack actuators and ensured that they were not subject to tension loads. The voltage of the top actuators was increased and the bottom actuators synchronously decreased in steps of 100 V, and the upward tip displacement (due to airfoil cambering) was recorded. At each point, the static airfoil tip displacement was recorded. This process was continued until the voltage applied to the top actuators reached 1000 V and the bottom actuators reached a voltage of 0 V. Next, the same procedure was repeated except that the bottom voltage was increased, whereas the top was decreased. This time, the downward tip displacement was measured. The results of the static test are shown in Fig. 31. The experimental results gave a static displacement at the maximum voltage of 3.65 mm at 1000 V. The ANSYS prediction of 3.69 mm compares very well (within 1.1%) with the experimental result.

Dynamic Test

The natural frequency as predicted by the ANSYS model was 40.1 Hz. It should be noted that no damping was present in the ANSYS model, and so it can only be used to predict the natural frequency, but not the amplitude of the dynamic response. The test setup for the dynamic test is very similar to the static test, except that the tip displacement for the dynamic test was measured using an accelerometer instead of a dial indicator. Again, a bias voltage of 500 V was used. For this test, two sine waves were generated, each with an amplitude of 500 V and 180 deg out of phase. One signal was sent to the top actuators and one to the bottom actuators. The frequency of the sine waves could be controlled, but was the same for both signals. The dynamic response for five trials ranging from 20–50 Hz is shown in Fig. 32, in which each set of data on the graph corresponds to one trial. The average resonant frequency for the prototype was found to be 38.75 Hz. This agrees closely with the ANSYS prediction of 40.1 Hz.

Conclusions

The shape optimization method described in this work details the design optimization of four compliant-mechanism units with distributed passive compliant material, along with five pairs of piezoelectric stack actuators, capable of producing moderate camber deflections. The shape optimization problem is formulated using both a single-criteria and multicriteria optimization approach designed to generate a structure that is compliant enough to minimize the required actuator forces yet stiff enough to resist the aerodynamic loads. A sequential linear programming algorithm was used to implement the shape optimization. A symmetrical compliant-mechanism structure aft of a rigid leading-edge D-spar provides stroke amplification to the piezoelectric actuators. The deformations due to the actuator forces and the aerodynamic loads are calculated using finite element analysis. The effect of passive-material area constraints and compliant-mechanism aspect ratio on the optimal solution was studied. It was found that as the passive-material constraint increased, the ratio of the tip deflection due to actuation to the tip deflection due to the airloads increased for both the TD and ratio objective functions. It was also found that the deflection due to the aerodynamic loads decreased for both objective functions, but was more pronounced for the ratio objective function. In general, as the compliant-mechanism aspect ratio decreased, the deflection due to actuation increased. However, for the ratio objective, the optimal aspect ratio fell between 20-30%, depending on the passive-material constraint.

For a compliant-mechanism aspect ratio of 30% and a passive-material limit of 50% of $A_{\max}$, the optimized shape using the ratio objective was predicted to achieve a trailing-edge deflection under actuation of 3.7 mm (an equivalent 15% trailing-edge flap deflection of 2.84 deg), and the optimized shape using the TD objective was predicted to achieve a trailing-edge deflection of 6.0 mm (a 4.6-deg equivalent trailing-edge flap angle). The optimized solutions were

found to be independent of the starting point, suggesting that the algorithm converges to a global optimum solution.

Comparing the two approaches (TD objective to ratio objective), it is seen that using the ratio objective function, the ratio of the actuation deflection to the deflection due to the aerodynamic loads is significantly higher. Additionally, the deflection due to the airloads is significantly lower, especially for larger passive volume constraints. However, the amount of tip deflection for the ratio objective function is significantly lower than is predicted with the TD objective function. This is because the ratio objective function takes the aerodynamic deflections into account, and the whole structure is made stiffer. An optimized solution using the TD objective function is a structure that is somewhat less stiff and consequently allows larger deflections under actuation. This is highly desirable. Although the deflections under aerodynamic loads are also larger (compared with those from the ratio objective function designs), these may still be small enough to be acceptable. Using the TD objective function, vertical tip deflections in the range of 6 to 8 mm are possible, resulting in a predicted increase in lift of 17–22%.

A bench-top prototype of the conformable airfoil was constructed. The static test of the prototype achieved a tip deflection of 3.65 mm, which was very close to the ANSYS prediction of 3.69 mm. The dynamic testing of the prototype showed the natural frequency to be 38.75 Hz, which was also close to the ANSYS prediction of 40.1 Hz.

Appendix: Design Sensitivities

To determine the sensitivity of the objective function, several derivations are required. The partial derivative of a displacement vector u with respect to a variable t_i can be derived from the expansion of the partial derivative of a general equilibrium equation relating the displacement vector u to a stiffness matrix K and a force vector f, as shown in Eq. (A1):

$$\frac{\partial(Ku)}{\partial t_i} = \frac{\partial f}{\partial t_i} \rightarrow \frac{\partial u}{\partial t_i} = K^{-1}\left(\frac{\partial f}{\partial t_i} - \frac{\partial K}{\partial t_i}u\right) \tag{A1}$$

The actuation force f_{act} and the aerodynamic force f_{air} are independent of the design variables, resulting in their sensitivities being zero, as shown in Eq. (A2):

$$\frac{\partial f_{\text{act}}}{\partial t_i} = 0 \qquad \frac{\partial f_{\text{air}}}{\partial t_i} = 0 \tag{A2}$$

The sensitivity of the global stiffness matrix is calculated by taking the derivative of the local stiffness matrices with respect to the passive-element stiffness, as shown in Eq. (A3) and then assembling them into the global matrix $\partial k/\partial t_i$:

$$\frac{\partial k_i}{\partial t_i} = L^T \begin{bmatrix} \frac{E}{l} & 0 & 0 & -\frac{E}{l} & 0 & 0 \\ 0 & \frac{3Et^2}{l^3} & \frac{3Et^2}{2l^2} & 0 & -\frac{3Et^2}{l^3} & -\frac{3Et^2}{2l^2} \\ 0 & \frac{3Et^2}{2l^2} & \frac{Et^2}{l} & 0 & -\frac{3Et^2}{2l^2} & \frac{Et^2}{2l} \\ -\frac{Et}{l} & 0 & 0 & \frac{Et}{l} & 0 & 0 \\ 0 & -\frac{3Et^2}{l^3} & -\frac{3Et^2}{2l^2} & 0 & \frac{3Et^2}{l^3} & -\frac{3Et^2}{2l^2} \\ 0 & \frac{3Et^2}{2l^2} & \frac{Et^2}{2l} & 0 & -\frac{3Et^2}{2l^2} & \frac{Et^2}{l} \end{bmatrix} L \tag{A3}$$

Combining expressions in Eqs. (A1) and (A2), we find that the sensitivity of the two displacement fields u_{act} and u_{air} corresponding to our design problem are given by the expressions in Eq. (A4):

$$\frac{\partial u_{\text{act}}}{\partial t_i} = -K^{-1}\frac{\partial K}{\partial t_i}u_{\text{act}} \qquad \frac{\partial u_{\text{air}}}{\partial t_i} = -K^{-1}\frac{\partial K}{\partial t_i}u_{\text{air}} \tag{A4}$$

Using a simple chain-rule approach and substituting the results from equation, we can derive the sensitivity of the tip deflection [Eq. (A5)] and the strain energy [Eq. (A6)]:

$$\frac{\partial \text{TD}}{\partial t_i} = \frac{(u_{\text{act}})_{\text{tip}}}{\partial t_i} \qquad \frac{\partial \text{TD}}{\partial t_i} = -K^{-1}\left(\frac{\partial K}{\partial t_i}\right)_{\text{tip}}(u_{\text{act}})_{\text{tip}} \tag{A5}$$

$$\begin{aligned} \frac{\partial \text{SE}}{\partial t_i} &= \frac{1}{2}\left[2u_{\text{air}}^T K\left(-K^{-1}\frac{\partial K}{\partial t_i}u_{\text{air}}\right) + u_{\text{air}}^T\frac{\partial K}{\partial t_i}u_{\text{air}}\right] \\ \frac{\partial \text{SE}}{\partial t_i} &= -\frac{1}{2}\left[u_{\text{air}}^T\frac{\partial K}{\partial t_i}u_{\text{air}}\right] \end{aligned} \tag{A6}$$

Finally, the sensitivity of the objective function is calculated using Eq. (A7), which is then expanded by simple substitution into the expression in Eq. (A8). The sensitivity of the TD objective function is given in Eq. (A5).

$$\frac{\partial(\text{TD}/\text{SE})}{\partial t_i} = \frac{(\text{SE})\frac{\partial(\text{TD})}{\partial t_i} - (\text{TD})\frac{\partial(\text{SE})}{\partial t_i}}{(\text{SE})^2} \tag{A7}$$

$$\begin{aligned} \frac{\partial(\text{TD}/\text{SE})}{\partial t_i} &= \frac{(\frac{1}{2}u_{\text{air}}^T K u_{\text{air}})[K^{-1}\frac{\partial K}{\partial t_i}(u_{\text{act}})_{\text{tip}}]}{(\frac{1}{2}u_{\text{air}}^T K u_{\text{air}})^2} \\ &+ \frac{(u_{\text{act}})_{\text{tip}}(-\frac{1}{2}u_{\text{air}}^T\frac{\partial K}{\partial t_i}u_{\text{air}})}{(\frac{1}{2}u_{\text{air}}^T K u_{\text{air}})^2} \end{aligned} \tag{A8}$$

Acknowledgment

The authors gratefully acknowledge the support of the National Rotorcraft Technology Center through the Pennsylvania State University Rotorcraft Center of Excellence.

References

[1] Milgram, J., Chopra, I., and Straub, F., "Rotors with Trailing Edge Flaps: Analysis and Comparison with Experimental Data," *Journal of the American Helicopter Society*, Vol. 43, No. 4, 1998, pp. 319–332.

[2] Bernhard, A. P. F., and Chopra, I., "Hover Testing of Active Rotor Blade-Tips Using a Piezo-Induced Bending-Torsion Coupled Beam," *Journal of Intelligent Material Systems and Structures*, Vol. 9, No. 12, 1999, pp. 963–974.

[3] Myrtle, T., and Friedmann, P., "Application of a New Compressible Time Domain Aerodynamic Model to Vibration Reduction in Helicopters Using an Actively Controlled Flap," *Journal of the American Helicopter Society*, Vol. 46, No. 1, 2001, pp. 32–43.

[4] Straub, F., and King, R., "Application of Smart Materials to Control of a Helicopter Rotor," *Proceedings of the Conference on Smart Structures and Materials*, Society of Photo-Optical Instrumentation Engineers, Bellingham, WA, Vol. 2721, 1996, pp. 66–77.

[5] Lee, T., and Chopra, I., "Design Issues of a High-Stroke, On-Blade Piezostack Actuator for a Helicopter Rotor with Trailing-Edge Flaps," *Journal of Intelligent Material Systems and Structures*, Vol. 11, No. 5, 2000, pp. 328–342.

[6] Clement, J. W., Brei, D., and Barret, R., "Wind Tunnel Testing of a High Authority Airspeed Insensitive Rotor Blade Flap," AIAA Paper 99-1503, Apr. 1999.

[7] Chattopadhyay, A., Seeley, C. E., and Mitchell, L., "Design of A Smart Flap Using Polymeric C-Block Actuators and A Hybrid Optimization Technique," *Smart Materials and Structures*, Vol. 6, No. 2, 1997, pp. 134–144.
doi:10.1088/0964-1726/6/2/002

[8] Hall, S., and Tzianetopoulou, T., "Design and Testing of a Double X-Frame Piezoelectric Actuator," *Proceedings of the Conference on Smart Structures and Materials*, Society of Photo-Optical Instrumentation Engineers, Bellingham, WA, Vol. 3985, 2000, pp. 26–37.

[9] Straub, F., Ngo, H. T., Anand, V., and Domzalski, D., "Development of a Piezoelectric Actuator for Trailing Edge Flap Control of Full Scale Rotor Blades," *Smart Materials and Structures*, Vol. 10, No. 1, 2001, pp. 25–34.
doi:10.1088/0964-1726/10/1/303

[10] Koratkar, N. A., and Chopra, I., "Wind Tunnel Testing of a Smart Rotor Model with Trailing-Edge Flaps," *Journal of the American Helicopter Society*, Vol. 47, No. 4, 2002, pp. 263–272.

[11] Fulton, M., and Ormiston, R. A., "Hover Testing of a Small-Scale Rotor with On-Blade Elevons," *Journal of the American Helicopter Society*, Vol. 46, No. 2, 2001, pp. 96–106.

[12] Saggere, l., and Kota, S., "Static Shape Control of Smart Structures Using Compliant Mechanisms," *AIAA Journal*, Vol. 37, No. 5, 1999, pp. 572–578.
[13] Hetrick, J., and Kota, S., "Energy Formulation for Parametric Size and Shape Optimization of Compliant Mechanisms," *Journal of Mechanical Design*, Vol. 121, No. 2, 1999, pp. 229–234.
[14] Xu, D., and Ananthasuresh, G. K., "Freeform Skeletal Shape Optimization of Compliant Mechanisms," *Journal of Mechanical Design*, Vol. 125, No. 2, 2003, pp. 253–261. doi:10.1115/1.1563634
[15] Rediniotis, O. K., Wilson, L. N., Lagoudas D. C., and Khan, M. M., "Development of a Shape-Memory-Alloy Actuated Biomimetic Hydrofoil," *Journal of Intelligent Material Systems and Structures*, Vol. 13, No. 1, 2002, pp. 35–49.
[16] Kudva, J., Sanders, B., Pinkerton-Florance, J., and Garcia, E., "Overview of DARPA/AFRL/NASA Smart Wing Phase 2 Program," *Proceedings of the Conference on Smart Structures and Materials*, Vol. 4332, Society of Photo-Optical Instrumentation Engineers, Bellingham, WA, 2001, pp. 383–389.
[17] Raney, D., Montgomery, R., Green, L., and Park, M., "Flight Control Using Distributed Shape-Change Effector Arrays," AIAA Paper 2000-1560, Apr. 2000.
[18] Anusonti-Inthra, P. R., Frecker, M., and Gandhi, F., "Design of a Conformable Rotor Airfoil Using Distributed Piezoelectric Actuators," *AIAA Journal*, Vol. 43, No. 8, Aug. 2005, pp. 1684–1695.
[19] Abbot, I. H., and Von Doenhoff, A. E., *Theory of Wing Sections*, Dover, New York, 1959.
[20] Katz, J., and Plotkin, A., *Low-Speed Aerodynamics: From Wing Theory to Panel Methods*, McGraw–Hill, New York, 1991.
[21] Frecker, M., Ananthasuresh, G. K., Nishiwaki, S., Kikuchi, N., and Kota, S., "Topological Synthesis of Compliant Mechanisms Using Multi-Criteria Optimization," *Journal of Mechanical Design*, Vol. 119, No. 2, 1997, pp. 238–245.
[22] Drela, M., "XFOIL—An Analysis and Design System for Low Reynolds Number Airfoils," *Proceedings of the Low Reynolds Number Aerodynamics Conference*, Notre Dame, IN, 1989, pp. 1–12.

A. Messac
Associate Editor